Pion elastic and inelastic scattering from ^{48,50}Ti, ^{52}Cr, and ^{54,56}Fe at 180 MeV: Determination of neutron and proton multipole matrix elements

D. S. Oakley, M. J. Smithson, S. Mordechai,* and C. Fred Moore
University of Texas at Austin, Austin, Texas 78712

P. A. Seidl†
Argonne National Laboratory, Argonne, Illinois 60439

C. L. Morris, G. C. Idzorek, and Z. F. Wang‡
Los Alamos National Laboratory, Los Alamos, New Mexico 87545

R. Gilman,§ J. D. Zumbro, and H. T. Fortune
University of Pennsylvania, Philadelphia, Pennsylvania 19104

S. J. Seestrom-Morris**
University of Minnesota, Minneapolis, Minnesota 55455

K. S. Dhuga
New Mexico State University, Las Cruces, New Mexico 88003

D. L. Watson††
University of Bradford, Bradford BD7 1DP, United Kingdom
and Los Alamos National Laboratory, Los Alamos, New Mexico 87545

(Received 28 August 1986)

Differential cross sections were measured for pion elastic and inelastic scattering from ^{48,50}Ti, ^{52}Cr, and ^{54,56}Fe at $T_\pi = 180$ MeV. Elastic scattering data were analyzed using a standard Kisslinger potential. Inelastic scattering data were analyzed using distorted-wave impulse-approximation calculations with collective-model transition densities. Ground-state neutron density parameters and matrix elements for some of the transitions were extracted and π^+/π^- differences investigated.

I. INTRODUCTION

Recent theoretical and experimental studies[1–7] have focused on the comparison of neutron and proton matrix elements, M_n and M_p, for inelastic transitions. The ratio of these two quantities, which is useful in testing various nuclear models, can be measured by hadronic probes that exist in isotopic multiplets, such as pions. In a previous study[1] both collective and microscopic form factors were used to analyze pion inelastic-scattering data. The resulting ratios, M_n/M_p, for the two different models were comparable within error, showing the possible model independence of such measurements.

In the present work we have used π^+ and π^- scattering at 180 MeV (near the $\Delta_{3/2,3/2}$ resonance) to study elastic and inelastic scattering from ^{48,50}Ti, ^{52}Cr, and ^{54,56}Fe. Our aim is a systematic study of M_n/M_p near the $N=28$ $f_{7/2}$ neutron subshell closure. Angular distributions have been compared with distorted-wave impulse-approximation (DWIA) calculations using collective-model transition densities. Such calculations have, in the past, been in relatively good agreement with experiment.[1,6–9]

For the strong collective states we have extracted the proton and neutron transition strengths. The proton matrix elements are compared with those resulting from electromagnetic measurements.

II. EXPERIMENT

A. Data acquisition

Data were collected using the Energetic Pion Channel and Spectrometer (EPICS) system at the Los Alamos Clinton P. Anderson Meson Physics Facility (LAMPF).[10] The EPICS system consists of a momentum-dispersing channel and a high resolution spectrometer. Position-sensitive delay-line read-out drift chambers measure the particle positions and angles, while an on-line computer program reconstructs the scattering angle and incident pion momentum, and calculates the scattered pion momentum.[1,6,8,9] The Q value for the reaction is then stored in a pion energy-loss spectrum as shown in Fig. 1.

Data were obtained with a channel momentum spread of $\pm 2\%$, while the flux was monitored by ion chambers downstream from the target. The scattering angle acceptance was about $\pm 1.5°$ and the momentum acceptance was $\pm 6\%$, corresponding to a 30-MeV region of excitation energy in the energy-loss spectra. Data were taken at scattering angles between $\theta_{lab} = 18°$ and 55° at an incident

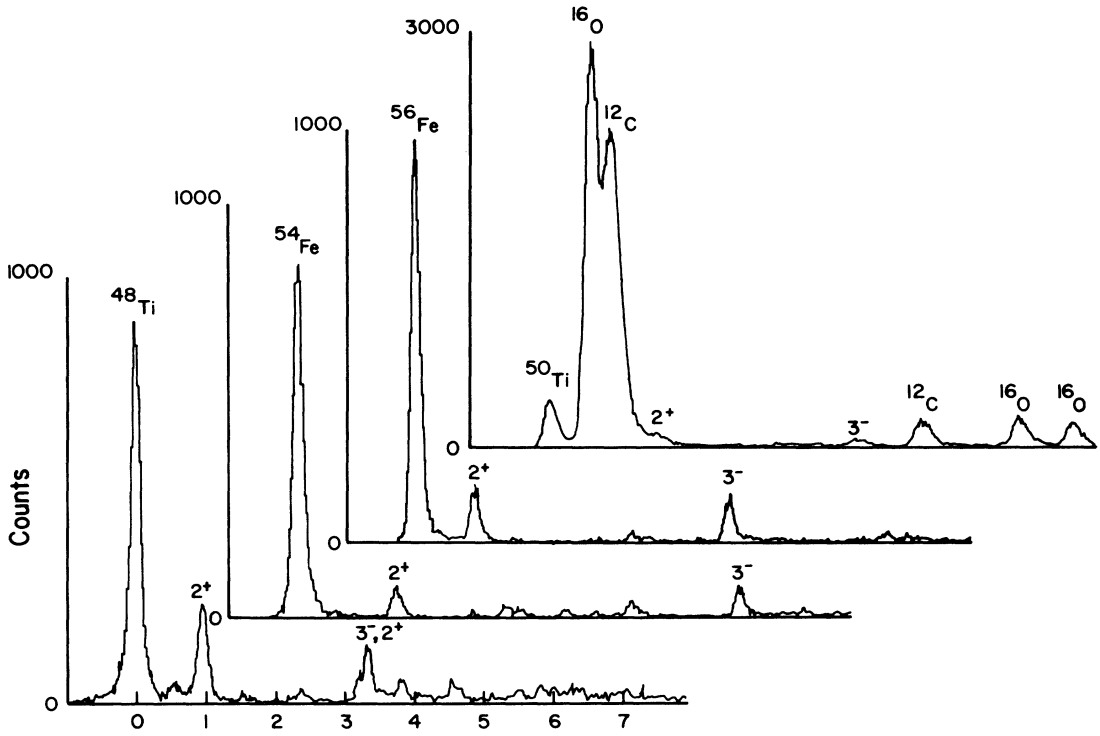

FIG. 1. Typical pion energy spectra at $\theta_{lab}=33°$.

pion energy of 180 MeV.

Because of the limited amount of target material, ^{54,56}Fe and ^{48,50}Ti were measured simultaneously as strip targets in the incident beam. Software gates on the target position separated interactions from the different target strips. The areal density, isotopic purity, and chemical purity of each target are given in Table I. Of the isotopically enriched targets, ^{50}Ti and ^{54}Fe, the ^{50}Ti had to be bound with 1.18 g of epoxy, thus introducing large oxygen, carbon, and hydrogen impurities (Fig. 1), while the remaining targets were all of natural abundance.

B. Data reduction

Peak areas were extracted from the pion energy-loss spectra by using the program FIT.[11] The peaks were fitted with a fixed line shape extracted from the elastic peaks.

TABLE I. Target specifications.

Target	Areal density (mg/cm^2)	Isotopic purity (%)	Chemical purity (%)
^{48}Ti	58.0	73.7	99.7
^{50}Ti[a]	148.4	67.5	99.7
^{52}Cr	122.7	83.8	99.2
^{54}Fe	95.4	97.6	98.3
^{56}Fe	92.2	91.8	99.3

[a]Values before epoxy added.

The relative energy separations of the various states were constrained at known excitation energies,[12–16] while their areas (cross sections) were varied until optimized by the program. Only prominent peaks, chosen by inspection of the spectra, were included. Because of the resolution, typically 150 keV [full width at half maximum (FWHM)], peaks for states that were within 60 keV of one another were considered as a single peak in the fitting procedure.

The data were normalized by comparing yields from π^+ and π^- scattering from hydrogen to π-p cross sections calculated with the program CROSS,[17] which utilizes the Coulomb-corrected phase shifts of Rowe *et al.*[18] The uncertainty in overall normalization was ±8%, consistent with systematic errors described below. Each strip target was individually normalized by putting the same software gates on the CH_2 (hydrogen) target positions as on the strip targets.

The data were corrected for the relative variation of solid angle as a function of position along the focal plane of the spectrometer by mapping the focal plane (acceptance scan) using elastic scattering from ^{93}Nb. As with the normalization, the acceptance scan was done with target cuts identical to those used with the strip targets. The data were also corrected for computer live time and chamber efficiency, which were monitored on line.

Estimated systematic uncertainties include normalization error, ±3%; focal plane variation of solid angle, ±2%; survival fraction correction, ±3%; chamber efficiency (angle dependent), ±3%; peak shape fitting errors, ±5%; beam monitoring, ±3%; giving an overall uncertainty of ±8%.

TABLE II. Ground-state density distribution parameters.[a]

Nucleus	$\{r^2\}_p^{1/2}$ (fm)	$\{r^2\}_n^{1/2}$ (fm)	c_p (fm)	c_n (fm)	a_p (fm)	a_n (fm)
^{48}Ti	3.49	3.48	3.85	3.80	0.49	0.50
^{50}Ti	3.50	3.53	3.92	3.90	0.47	0.49
^{52}Cr	3.57	3.57	3.98	3.90	0.48	0.51
^{54}Fe	3.64	3.60	4.01	3.90	0.51	0.53
^{56}Fe	3.70	3.61	3.97	4.00	0.55	0.50

[a]$E^{\text{shift}} = -28.0$ MeV.

III. ANALYSIS

A. Elastic scattering

The coordinate-space computer code DWPI (Ref. 19) was used to generate both elastic and inelastic distorted-wave impulse-approximation (DWIA) calculations. All calculations used the Kisslinger[20] form for the pion-nucleus potential. An empirical energy shift[21] of -28.0 MeV was included in the optical-model potential.

The neutron and proton ground-state densities were parametrized with a Woods-Saxon distribution,

$$\rho(r)=\rho_0(1+e^{(r-c)/a})^{-1} .$$

For the proton distributions, the half-density radius, c_p, and the root-mean-square (rms) charge radius, $\langle r^2\rangle_z^{1/2}$, were taken from previous experiments.[22–25] The diffuseness, a_p, is related to c_p and the rms point proton distribution, $\langle r^2\rangle_p^{1/2}$, by[26]

$$a_p^2 \cong 5(\langle r^2\rangle_p - \tfrac{3}{5}c_p^2)/7\pi^2 ,$$

where

$$\langle r^2\rangle_p = [\langle r^2\rangle_z - (0.8)^2]^{1/2} .$$

The neutron parameters were varied to obtain a best fit to the data. Although use of the same geometry for neutrons and protons fit the π^- distributions reasonably well, the neutron diffuseness generally had to be altered in order to fit the second maxima optimally. These resulting parameters are listed in Table II, and the elastic-scattering angular distributions are presented in Fig. 2.

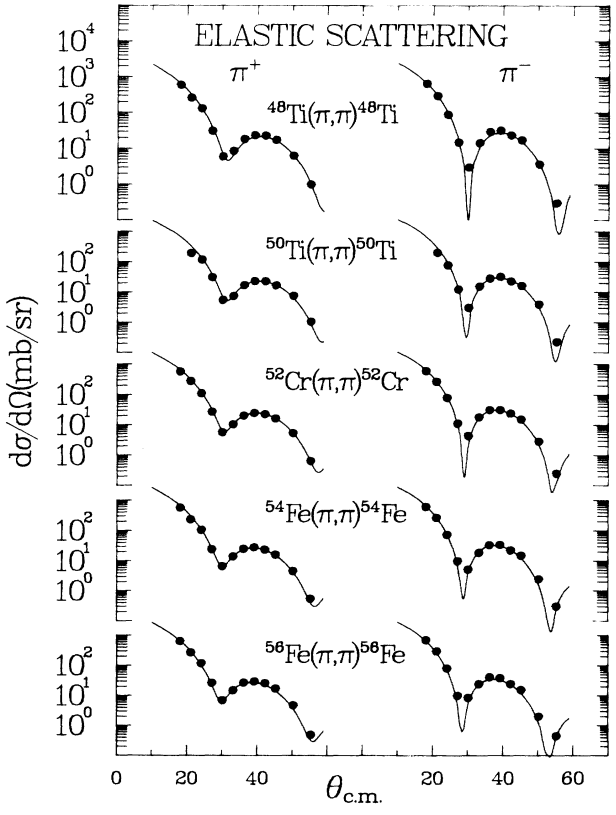

FIG. 2. Elastic-scattering angular distributions. The solid curves represent DWPI calculations.

B. Inelastic scattering

Collective-model transition densities were used to analyze the inelastic data. Tassie-model form factors[27]

TABLE III. Comparison of electromagnetic transition strengths from this experiment and electromagnetic measurements. All units are Weisskopf single-particle units.

Nucleus	State	$B(El)$[a]	$B(El)$[b]
^{48}Ti	2_1^+	13.4 (1.0)	13.0 (1.0)
	2_2^+	1.11 (0.21)	1.20 (0.20)
^{50}Ti	2_1^+	6.54 (0.56)	5.80 (0.40)
^{52}Cr	2_1^+	10.2 (0.38)	11.0 (1.0)
	2_2^+		0.02 (0.01)
	2_3^+		0.20 (0.07)
	2_4^+	1.65 (0.13)	0.14 (0.07)
	4_1^+	3.10 (0.48)	3.40 (0.60)
	3_1^-	6.08 (0.45)	6.10 (0.30)
^{54}Fe	2_1^+	7.81 (0.73)	8.30 (0.20)
	2_2^+	2.67 (0.26)	2.10 (0.30)
	2_3^+	1.75 (0.40)	0.72 (0.15)
^{56}Fe	2_1^+	14.9 (0.62)	16.0 (1.0)
	2_2^+	1.16 (0.24)	0.27 (0.07)
	2_3^+		0.16 (0.05)

[a]States with no entries have unusually shaped angular distributions and strengths were not extracted.
[b]Values are from Ref. 30 (see also Refs. 32 and 33).

TABLE IV. Neutron and proton multipole matrix elements extracted for ^{48,50}Ti from this work. All units are Weisskopf single-particle units, with the conversion to $e^2\,\mathrm{fm}^{2l}$ as given.

Nucleus	State (J^π)	E_x (MeV)	M_p (W.u.)$^{1/2}$	M_n (W.u.)$^{1/2}$	W.u. $(e^2\,\mathrm{fm}^{2l})$	$(M_n/M_p)/(N/Z)$
^{48}Ti	2_1^+	0.98	3.66 (0.14)	4.38 (0.10)	51.8	1.01 (0.05)
	2_2^+	2.42	1.05 (0.10)	0.81 (0.15)	51.8	0.65 (0.14)
	2_3^+	3.37	1.14 (0.12)	1.05 (0.09)	51.8	0.78 (0.11)
	2^+	3.63	0.48 (0.13)	0.56 (0.13)	51.8	0.98 (0.36)
	2^+	4.39	0.53 (0.06)	0.76 (0.14)	51.8	
	2^+	5.62	0.63 (0.12)	0.88 (0.17)	51.8	
	2^+	6.10	0.68 (0.15)	0.98 (0.21)	51.8	
	3_1^-	3.36	2.17 (0.10)	2.36 (0.14)	958	
	3_2^-	3.85	1.70 (0.09)	1.73 (0.21)	958	
	3_3^-	4.58	1.59 (0.10)	1.63 (0.19)	958	
	3^-	5.52	1.02 (0.15)	1.18 (0.22)	958	
	3^-	6.06	1.20 (0.15)	1.39 (0.16)	958	
	3^-	6.96	0.93 (0.11)	1.39 (0.18)	958	
	4^+	4.39	0.90 (0.15)	1.91 (0.22)	17 210	
^{50}Ti	2_1^+	1.55	2.56 (0.11)	2.24 (0.10)	54.7	0.69 (0.04)
	2_2^+	4.17	0.31 (0.16)	1.07 (0.10)	54.7	2.71 (1.42)
	2_3^+	4.31	1.10 (0.20)	1.11 (0.12)	54.7	0.79 (0.17)
	3_1^-	4.41	2.12 (0.10)	2.04 (0.13)	1040	
	4_1^+	2.68	1.67 (0.22)	1.60 (0.20)	19 190	

were also used for the ^{48}Ti 2_1^+ angular distribution for purposes of comparison and gave results similar to the collective-model calculations to within 10%. While the collective model should be expected to work reasonably well for the strong 2_1^+ states,[28] the single-particle aspects of the higher-lying states are likely to cause the transition densities for those states to have very different shapes. In this case, the collective model might not provide a good description of the angular distributions.

The strength parameters, β_n and β_p, were adjusted to both the π^+ and π^- data. The neutron and proton reduced multipole matrix elements are related to the transition densities by[29]

$$M(\mathrm{n}_l)=\int_0^\infty r^{l+2}\rho_{\mathrm{tr,n}}(r)dr$$

and

$$M(\mathrm{p}_l)=\int_0^\infty r^{l+2}\rho_{\mathrm{tr,p}}(r)dr\ ,$$

where

$$\rho_{\mathrm{tr}}(r)\sim\beta\frac{d\rho(r)}{dr}\ .$$

In the long-wavelength limit these are related to the electromagnetic strengths by

$$B(El,\ J_i\rightarrow J_f)=|\,M_{\mathrm{p}_l}\,|^2/(2J_i+1)\ .$$

The errors in the strength parameters, and thus the matrix elements, were determined from the statistical errors in the measured cross sections, $\Delta\sigma$, by

$$(\Delta\beta_p)^2=\left[\frac{d\beta_p}{d\sigma^+}\Delta\sigma^+\right]^2+\left[\frac{d\beta_p}{d\sigma^-}\Delta\sigma^-\right]^2\ ,$$

and similarly for β_n. Here, $\Delta\sigma$ was taken from a single data point at the first maximum where the superscripts refer to π^+ or π^- cross sections.

TABLE V. Neutron and proton multipole matrix elements extracted for ^{52}Cr from this work. All units are Weisskopf single-particle units, with the conversion to $e^2\,\mathrm{fm}^{2l}$ as given.

Nucleus	State (J^π)	E_x (MeV)	M_p (W.u.)$^{1/2}$	M_n (W.u.)$^{1/2}$	W.u. $(e^2\,\mathrm{fm}^{2l})$	$(M_n/M_p)/(N/Z)$
^{52}Cr	2_1^+	1.43	3.19 (0.06)	2.87 (0.06)	57.7	0.77 (0.02)
	2^+	3.77	1.29 (0.05)	1.88 (0.06)	57.7	
	3_1^+	4.56	2.47 (0.09)	2.48 (0.09)	1120	
	4_1^+	2.37	1.76 (0.13)	1.73 (0.13)	21 300	
	4_2^+	2.77	1.53 (0.08)	1.67 (0.14)	21 300	
	4_3^+	3.42	0.61 (0.05)	1.25 (0.09)	21 300	
	4_4^+	4.02	0.96 (0.10)	1.61 (0.10)	21 300	
	4^+	4.63	2.46 (0.33)	1.29 (0.19)	21 300	

TABLE VI. Neutron and proton multipole matrix elements extracted for ^{54,56}Fe from this work. All units are Weisskopf single-particle units, with the conversion to $e^2\,\mathrm{fm}^{2l}$ as given.

Nucleus	State (J^π)	E_x (MeV)	M_p (W.u.)$^{1/2}$	M_n (W.u.)$^{1/2}$	W.u. ($e^2\,\mathrm{fm}^{2l}$)	$(M_n/M_p)/(N/Z)$
^{54}Fe	2_1^+	1.41	2.80 (0.13)	2.78 (0.10)	60.6	0.92 (0.05)
	2_2^+	2.96	1.63 (0.08)	2.43 (0.10)	60.6	1.38 (0.10)
	2_3^+	3.17	1.32 (0.15)	1.03 (0.14)	60.6	0.72 (0.13)
	2_4^+	4.58	0.88 (0.14)	0.88 (0.12)	60.6	0.93 (0.20)
	3_1^-	4.78	1.80 (0.09)	1.57 (0.17)	1210	
	3_2^-	6.34	2.63 (0.10)	2.35 (0.20)	1210	
	4_1^+	2.54	1.98 (0.16)	1.19 (0.10)	23 560	
	4_2^+	3.30	0.89 (0.10)	1.72 (0.13)	23 560	
	4_3^+	3.83	2.23 (0.22)	2.02 (0.19)	23 560	
	4^+	4.95	1.32 (0.19)	1.36 (0.16)	23 560	
^{56}Fe	2_1^+	0.85	3.85 (0.08)	4.43 (0.10)	63.6	1.00 (0.03)
	2_2^+	2.66	1.08 (0.11)	1.65 (0.10)	63.6	1.32 (0.16)
	2_4^+	3.37	1.14 (0.08)	1.27 (0.12)	63.6	
	3_1^-	4.51	3.10 (0.08)	4.14 (0.12)	1300	
	4_1^+	2.09	0.62 (0.21)	1.00 (0.17)	25 960	
	4_2^+	3.12	2.48 (0.13)	2.68 (0.29)	25 960	
	4^+	4.12	1.33 (0.11)	1.17 (0.15)	25 960	

The inelastic angular distributions are presented in Figs. 3—11. The resulting electromagnetic strengths, listed in Table III, are, for purposes of comparison, given in Weisskopf single-particle units, where $B(El\uparrow)=B(El\downarrow)$. The matrix elements for selected transitions are listed in Tables IV—VI. These values were calculated both by setting the ground-state neutron parameters equal to the ground-state proton parameters, and also by setting the ground-state neutron parameters equal to the ground-state neutron parameters given in Table II. The resulting matrix elements were the same for both cases.

IV. RESULTS

A. ^{48}Ti

Angular distributions for the inelastic ^{48}Ti states are presented in Figs. 3 and 4. Most of the 2^+ and 3^- angular distributions presented for this nucleus are well described by collective-model calculations. The first two 2^+ states produce transition strengths that are in very good agreement with previous electromagnetic measurements (Table III).[30] A Tassie-model calculation for the 2_1^+ angular distribution gave similar results in shape and magnitude to the collective-model calculation.

The 3^- and 2^+ states at 3.36 and 3.37 MeV, respectively, could not be resolved from each other and a single state was fitted at 3.36 MeV. Similarly, a 2^+ at 3.63 MeV and the state at 3.62 MeV, which appears to be a 3^- in these data, was fitted at 3.63 MeV; other peaks at 4.05, 4.39, and 6.09 MeV were fitted. Tables VII—IX indicate the unresolved states contained in these peaks. The values of the matrix elements for the states at 3.36 and 3.37 MeV were obtained from the best fit obtained by adding 3^- and 2^+ calculations (Fig. 3).

The 2^+ angular distributions for the peak at 4.05 MeV are not described well with 2^+ collective-model calculations, perhaps partially because of the neighbor state at 4.04 MeV, a different transition density shape is necessary, or perhaps coupled-channel effects are important.

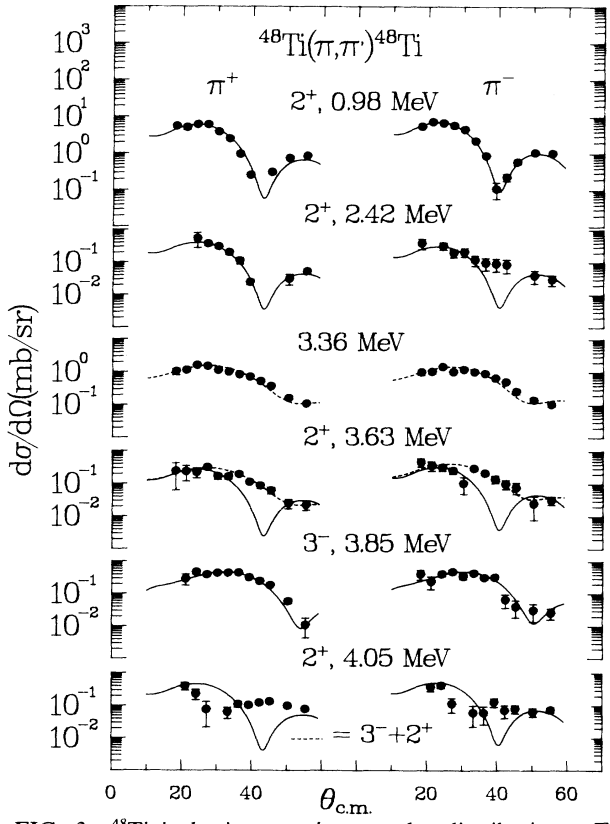

FIG. 3. ^{48}Ti inelastic-scattering angular distributions. The solid curves represent collective-model DWPI calculations and the dashed lines represent additive 2^+ and 3^- curves.

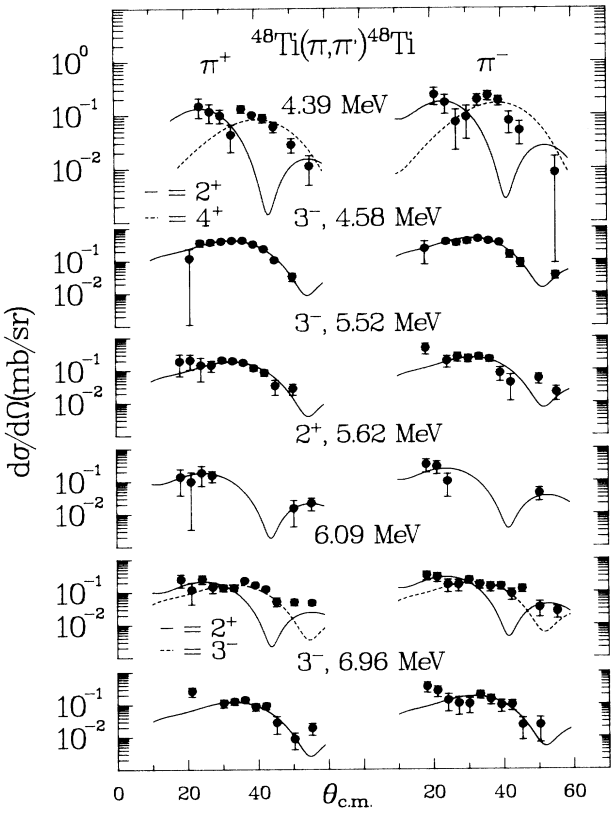

FIG. 4. ^{48}Ti inelastic-scattering angular distributions. The solid curves represent collective-model DWPI calculations and the dashed lines represent added states.

TABLE VII. ^{48,50}Ti states for which data are presented in this paper.

Nucleus	State (J^π)	E_x[a] (adopted MeV)	E_x[b] (MeV fit)
^{48}Ti	0$^+$	0.00	0.00
	2$^+$	0.98	0.98
	2$^+$	2.42	2.42
	3$^-$	3.36	3.36
	2$^+$	3.37	
	(2$^+$)	3.62	3.63
	2$^+$	3.63	
	3$^-$	3.85	3.87
	2$^+$	4.04	4.05
	(5$^-$)	4.06	
	2$^+$	4.07	
	4$^+$	4.38	4.39
	4$^+$	4.39	
	(2$^+$)	4.40	
	3$^-$	4.58	4.58
	3$^-$	5.52	5.54
	2$^+$	5.62	5.62
	3$^-$	6.06	6.09
	(2$^+$)	(6.10)	
	3$^-$	6.96	6.96
^{50}Ti	0$^+$	0.00	0.00
	2$^+$	1.55	1.56
	4$^+$	2.68	2.68
	(2$^+$)	(4.17)	4.18
	2$^+$	4.31	4.31
	3$^-$	4.41	4.41

[a]From Refs. 12 and 13.
[b]From this work. States fitted at the same energy are unresolved here.

B. ^{50}Ti

Angular distributions for the inelastic ^{50}Ti states are presented in Fig. 5. All of the 2$^+$ and 3$^-$ angular distributions in these data are well described by collective-model calculations; the first 2$^+$ state produces a transition strength that is in fairly good agreement with previous electromagnetic measurements (Table III).[30] The large impurities of oxygen and carbon in this target, however, made complete angular distributions from 18° to 55° impossible.

C. ^{52}Cr

Angular distributions for the inelastic ^{52}Cr states are presented in Figs. 6 and 7. The data for the first 3$^-$, 4$^+$, and 2$^+$ are well described by collective-model calculations. Measured transition strengths (Table III) agree very well with previous measurements,[30] except for the 2_4^+ state measured at 3.77 MeV, for which the present $B(E2)$ is a factor of 10 different from the electromagnetic value. This difference cannot be attributed to neighboring states or to contaminants. Other, more anomalously shaped angular distributions for this nucleus are discussed in a later section.

TABLE VIII. ^{52}Cr states for which data are presented in this paper.

Nucleus	State (J^π)	E_x[a] (adopted MeV)	E_x[b] (MeV fit)
^{52}Cr	0$^+$	0.00	0.00
	2$^+$	1.43	1.43
	4$^+$	2.37	2.37
	4$^+$	2.77	2.77
	2$^+$	2.96	2.96
	2$^+$	3.16	3.16
	(4$^+$)	3.42	3.42
	2$^+$	3.77	3.77
	4$^+$	4.04	4.04
	3$^-$	4.56	4.56
	(4$^+$)	4.63	4.63
	(5$^+$)	4.63	

[a]From Ref. 14.
[b]From this work. States fitted at the same energy are unresolved here.

TABLE IX. ^{54,56}Fe states for which data are presented in this paper.

Nucleus	State (J^π)	E_x[a] (adopted MeV)	E_x[b] (MeV fit)
^{54}Fe	0^+	0.00	0.00
	2^+	1.41	1.41
	4^+	2.54	2.54
	0^+	2.56	
	2^+	2.96	2.96
	2^+	3.17	3.17
	4^+	3.30	3.30
	4^+	3.83	3.83
	2^+	4.58	4.58
	3^-	4.78	4.78
	$4(^+)$	4.95	4.95
	3^-	6.34	6.34
^{56}Fe	0^+	0.00	0.00
	2^+	0.85	0.85
	4^+	2.09	2.09
	2^+	2.66	2.66
	0^+	2.94	2.96
	2^+	2.96	2.96
	1^+	3.12	3.12
	4^+	3.12	
	2^+	3.37	3.37
	2^+	3.60	3.60
	0^+	3.61	
	$(4)^+$	4.12	4.12
	3^-	4.51	4.51

[a]From Refs. 15 and 16.
[b]From this work. States fitted at the same energy are unresolved here.

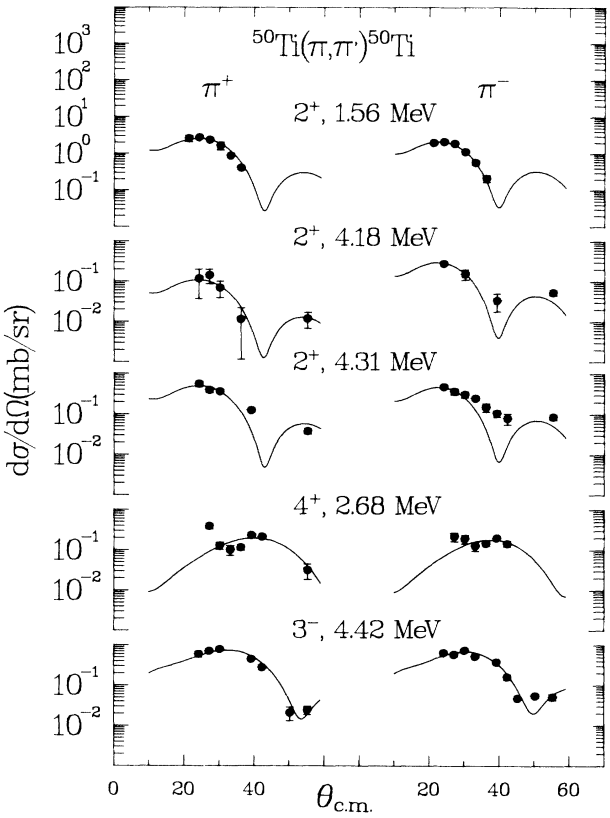

FIG. 5. ^{50}Ti inelastic-scattering angular distributions. The solid curves represent collective-model DWPI calculations.

D. ^{54}Fe

Angular distributions for the inelastic ^{54}Fe states are presented in Figs. 8 and 9. All of the 2^+, 3^-, and 4^+ angular distributions for this nucleus agree with collective-model calculations. The forward-angle rise for the 4_1^+ angular distribution might be partially due to the unresolved 0^+ state at 2.56 MeV. If the 0^+ is contributing, it is stronger in the π^- than in the π^+ data.

Measured transition strengths (Table III) compare reasonably well with previous measurements,[30] except for the 2_3^+ state at 3.17 MeV. The strength determined from this measurement is twice the strength reported in previous experiments and, as before, this discrepancy cannot be attributed to neighboring states or contaminants.

E. ^{56}Fe

Angular distributions for the inelastic ^{56}Fe states are presented in Figs. 10 and 11. As in the other nuclei, the first 2^+, 3^-, and 4^+ data presented for this nucleus are well described by collective-model calculations. The forward-angle peak in the 4_2^+ angular distribution might be due to an unresolved (1^+) state at 3.12 MeV, although it is unlikely that an unnatural-parity state would be strong enough to produce such a large forward-angle enhancement.

Measured transition strengths (Table III) compare reasonably well with previous measurements,[30] except for the 2_2^+ state at 2.66 MeV, which is a factor of 4 high, and once again this cannot be attributed to neighboring states or contaminants.

F. Mass dependence of the matrix elements

Figure 12 shows the matrix elements M_n,M_p, and their ratio, as a function of mass number (A), for the first 2^+ and 3^- states of the $N=28$ nuclei (^{48}Ca, ^{50}Ti, ^{52}Cr, and ^{54}Fe), and Fig. 13 shows M_n/M_p vs A for nuclei around $N=28$ (^{42,44,48}Ca, ^{48,50}Ti, ^{52}Cr, and ^{54,56}Fe). The $1f_{7/2}$ neutron and proton subshells in ^{48}Ti are only partially filled and the relative neutron and proton contributions to the first 3^- and 2^+ states are very close to those predicted by the collective model (i.e., N/Z, as in Table IV and Fig. 13). In ^{50}Ti the $1f_{7/2}$ neutron subshell is filled and there is less neutron contribution to both the 3_1^- state and the 2_1^+ state.

A smaller neutron contribution to the low-lying negative-parity states is expected because the shell closure

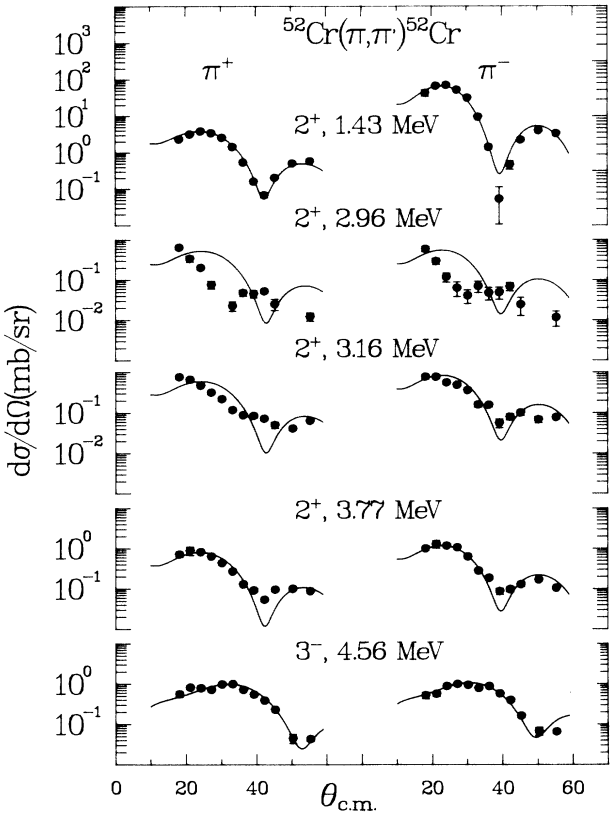

FIG. 6. ^{52}Cr inelastic-scattering angular distributions. The solid curves represent collective-model DWPI calculations.

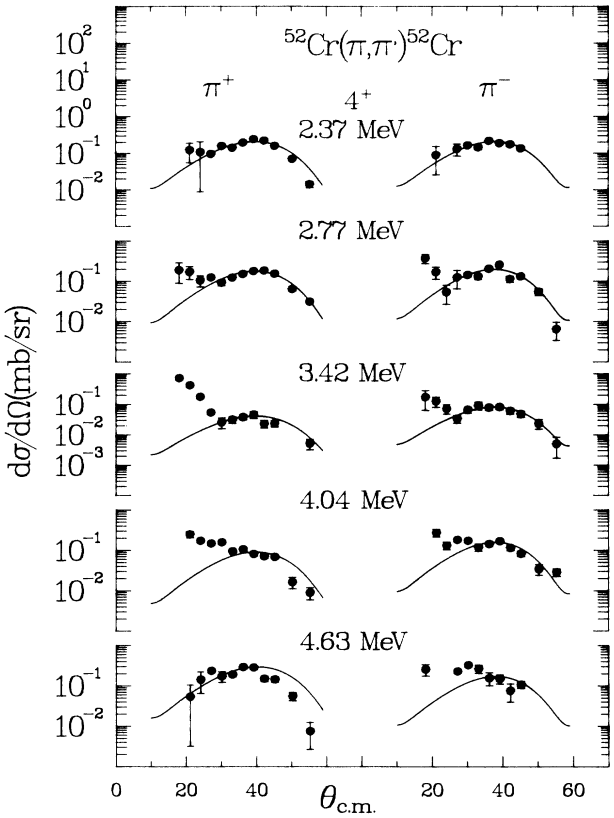

FIG. 7. ^{52}Cr inelastic-scattering angular distributions. The solid curves represent collective-model DWPI calculations.

inhibits valence neutron promotion from the lower *s-d* shell orbitals and thus prohibits these neutrons from forming negative-parity states in the $1f_{7/2}$ subshell. Neutron contribution to the low-lying positive-parity states can also be qualitatively explained. Part of the 2_1^+ state wave function can be formed by recoupling the $1f_{7/2}$ neutrons. As the subshell becomes filled, these recouplings are no longer possible and one might expect a reduced neutron contribution to these states. The neutrons in the $1f_{7/2}$ subshell, however, can still be promoted to the higher, negative-parity orbitals within the *f-p* shell, contributing to some neutron participation in forming positive-parity states. The decrease of M_n in ^{50}Ti 2_1^+ from that of ^{48}Ti 2_1^+ indicates the importance of the $f_{7/2}$ rearrangement, yet the opposite effect is seen in the 2_1^+ state of the $N=28$ nucleus ^{48}Ca,[1] where M_n is larger than in neighboring nuclei (Fig. 12).

As protons are added to the $N=28$ nuclei, from ^{50}Ti to ^{54}Fe, the neutron contribution to the 2_1^+ states apparently increases while the contribution to the lowest 3^- state does not. As more neutrons are then added, forming ^{56}Fe (Fig. 13), we see further increase of neutron contribution to both the 3_1^- and 2_1^+ states, as would be expected. As in ^{48}Ti, the relative neutron and proton contributions to the first 3^- and 2^+ states of ^{56}Fe are very close to that predicted by the collective model (Table VI, Fig. 13).

G. Relative π^+ and π^- cross sections and magnitudes

A reversal of the magnitude of $(M_n/M_p)/(N/Z)$ about unity between successive 2^+ states has been the subject of a previous study.[2] This reversal effect is seen clearly for the first two 2^+ states in ^{50}Ti and ^{54}Fe as shown in Tables IV and VI. A reversal of this quantity might also be seen in the first two 2^+ states and the second two 2^+ in ^{48}Ti, the second two 2^+ states in ^{54}Fe, and the first two 2^+ states in ^{56}Fe. The ratios in these states, however, are often close to unity, making it hard to tell with certainty if the effect is seen.

The π^+ and π^- cross sections for the first two 2^+ states for these nuclei are compared in Fig. 14. In this figure it can be seen that there is generally a reversal in magnitude of the π^+ and π^- cross sections between the first two 2^+ states, except for ^{56}Fe, where the π^- cross section is greater than that of the π^+ in both states.

H. Anomalously shaped angular distributions

The ^{52}Cr 2_2^+ angular distributions, for both π^+ and π^-, have minima that occur at dramatically smaller angles than in the first 2^+ state. This effect is not reproduced in

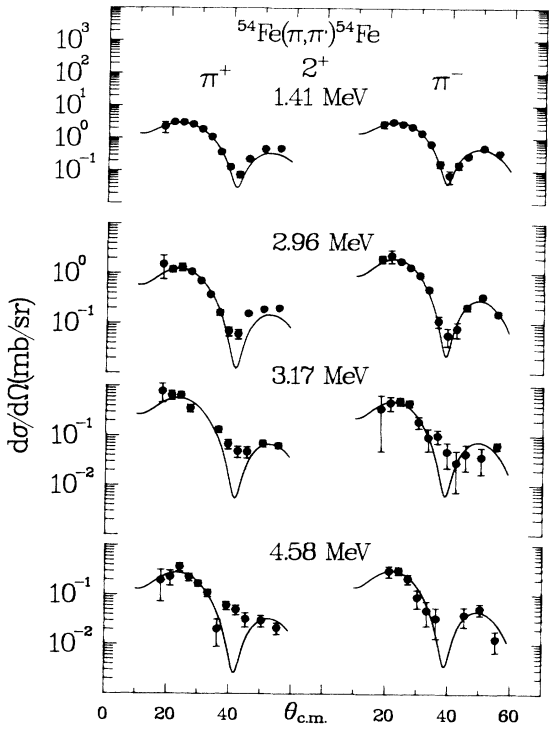

FIG. 8. ^{54}Fe inelastic-scattering angular distributions. The solid curves represent collective-model DWPI calculations.

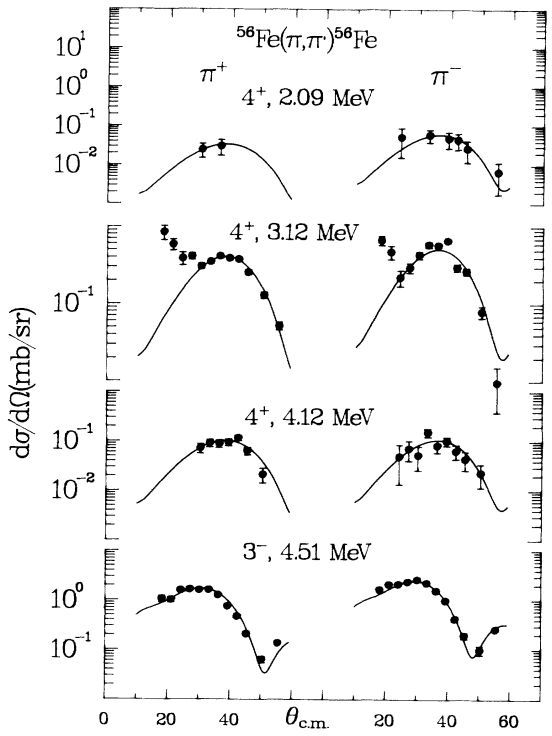

FIG. 10. ^{56}Fe inelastic-scattering angular distributions. The solid curves represent collective-model DWPI calculations and the dashed lines represent additive 2^+ and 0^+ curves.

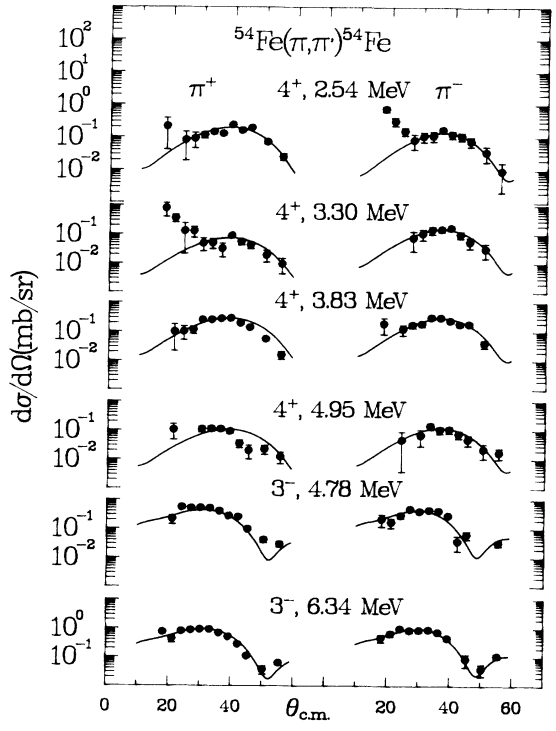

FIG. 9. ^{54}Fe inelastic-scattering angular distributions. The solid curves represent collective-model DWPI calculations.

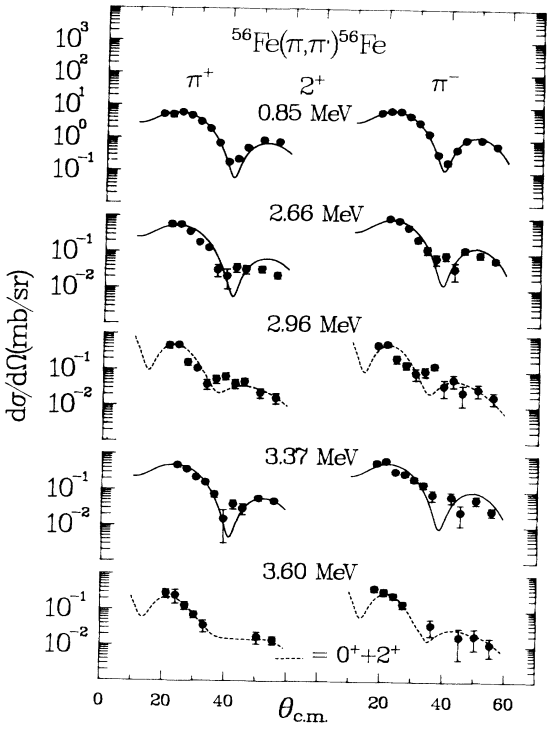

FIG. 11. ^{56}Fe inelastic-scattering angular distributions. The solid curves represent collective-model DWPI calculations.

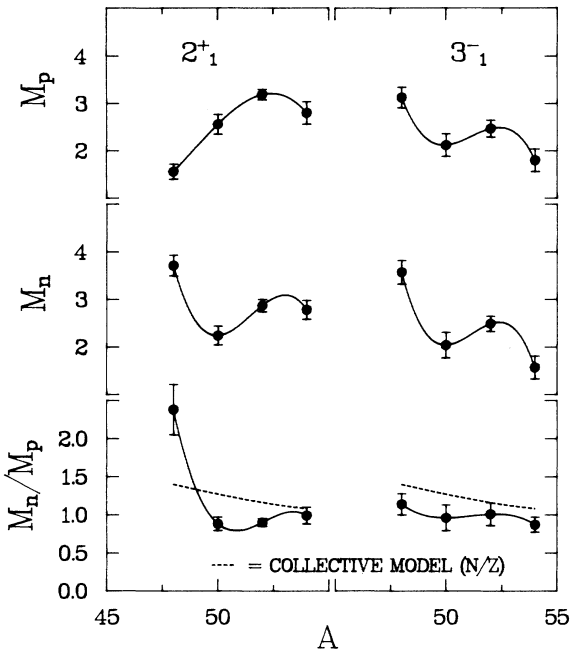

FIG. 12. Matrix elements vs mass (A) for the $N=28$ nuclei ^{48}Ca, ^{50}Ti, ^{52}Cr, and ^{54}Fe. The solid lines connect the data points. (Calcium data are from Ref. 1.)

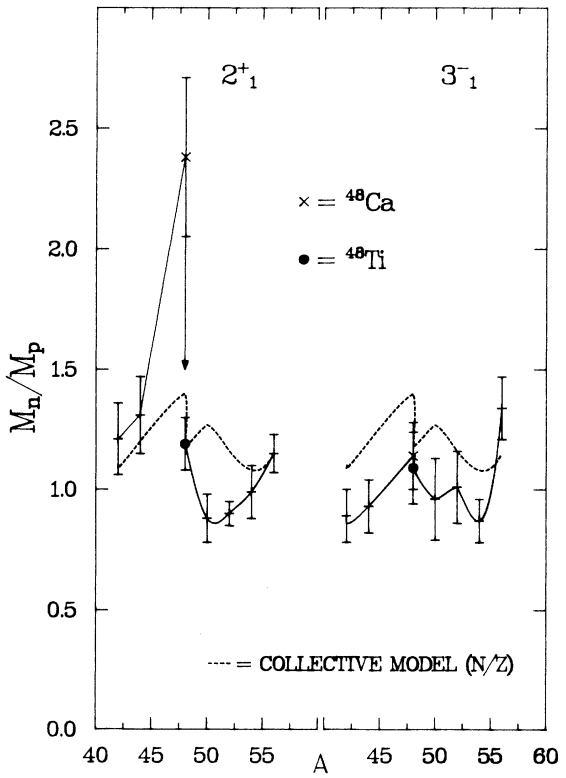

FIG. 13. M_n/M_p, for the first 2^+ and 3^- states, vs mass (A) for nuclei around $N=28$: ^{42}Ca, ^{44}Ca, ^{48}Ca, ^{48}Ti, ^{50}Ti, ^{52}Cr, ^{54}Fe, and ^{56}Fe. The solid lines connect the data points. (Calcium data are from Ref. 1.)

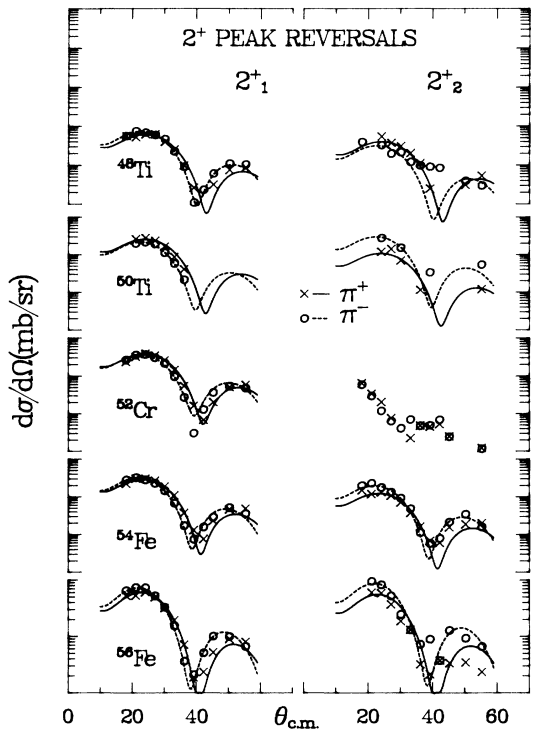

FIG. 14. π^+/π^- comparisons of inelastic-scattering angular distributions to the 2^+_1 and 2^+_2 states. The solid and dashed curves represent collective-model DWPI calculations for π^+ and π^-, respectively.

the calculations. A similar effect is possibly present in the 2^+_3 angular distributions of this nucleus as well as for the 2^+ (4.05 MeV) state in ^{48}Ti, and possibly the 2^+_2 and 2^+_3 levels in ^{56}Fe. Even though a 0^+ state is unresolved from the 2^+_3 in ^{59}Fe, the second maximum is still not reproduced by a sum of 2^+ and 0^+ calculations. These angular distributions can be reproduced by changing the form factors (in an extreme way), but this is unlikely to give a complete explanation of the shapes.

The feature that these states have in common is an unusually weak transition strength to the ground state and also a strong transition strength to some intermediate state,[30] indicating the possible importance of coupled-channel effects.

Many of the 4^+ angular distributions in these nuclei (2.77, 3.42, 4.04, 2.37, and 4.63 MeV in ^{52}Cr; 3.30, 2.54, 3.83, and 4.95 MeV in ^{54}Fe; and 3.12 MeV in ^{56}Fe) are described well by collective-model calculations, except for a forward-angle peaking. The ^{52}Cr 4^+_3 angular distribution, measured at 3.42 MeV, for example, is very similar in shape to that of the 2^+_2 distribution. This peaking, with the possible exception of the ^{54}Fe 4^+_1 and ^{56}Fe 4^+_2 states, cannot be attributed to normal background or contaminants.

Further investigation into the EPICS channel, however, has revealed possible slit scattering from the front-end collimator.[31] This results in a broad second elastic peak at

forward angles with an apparent excitation energy of 2 to 4 MeV and with a magnitude of roughly 1% that of the elastic. This background should have little effect on peaks which are strong at forward angles, but not for the 4^+ states which are small in this region of large elastic cross section. Because of this uncertainty, the high forward peaking of these 4^+ states may not be a real effect. Further calculations of these anomalously shaped angular distributions are in progress.

V. CONCLUSION

Many of the inelastic transitions measured by pion scattering from the nuclei ^{48,50}Ti, ^{52}Cr, and ^{54,56}Fe can be described by DWIA calculations using collective-model transition densities. These collective-model calculations compare very well with most of the 2^+ and 3^- angular distributions presented, and the proton transition strengths, extracted for the prominent states, are in reasonable agreement with electromagnetic measurements. This agreement helps to validate the use of pions in measuring the multipole matrix elements for both neutrons and protons for such states. However, for higher lying states with small ground-state $B(E2)$ strengths, the matrix elements extracted from pion scattering appear to be consistently larger than those measured in gamma decay.

A reversal of the magnitude of the quantity $(M_n/M_p)/(N/Z)$ about unity between successive 2^+ states is seen in ^{50}Ti and ^{54}Fe, and possibly in ^{48}Ti and ^{56}Fe. Pauli blocking effects are also seen around the closure of the $f_{7/2}$ subshell.

Still to be explained are some of the ^{52}Cr and ^{56}Fe 2^+ data, the forward peak on the 4^+ data, and some differing strength values. Otherwise, these data are in fairly good agreement with theoretical calculations.

ACKNOWLEDGMENTS

This work was supported in part by the U.S. Department of Energy, The Robert A. Welch Foundation, and the National Science Foundation.

*Permanent address: Ben Gurion University of the Negev, Beer-Sheva, Israel.
†Present address: Lawrence Berkeley Laboratory, Berkeley, CA 94720.
‡Permanent address: Institute of Atomic Energy, Beijing, People's Republic of China.
§Present address: Argonne National Laboratory, Argonne, IL 60439.
**Present address: Los Alamos National Laboratory, Los Alamos, NM 87545.
††Present address: University of York, York Y01 5DD, United Kingdom.

[1]K. G. Boyer *et al.*, Phys. Rev. C **24**, 598 (1981).
[2]V. R. Brown, A. M. Bernstein, and V. A. Madsen, Phys. Lett. **164B**, 217 (1985).
[3]A. M. Bernstein, V. R. Brown, and V. A. Madsen, Phys. Rev. Lett. **42**, 425 (1979).
[4]A. M. Bernstein *et al.*, Phys. Rev. Lett. **49**, 451 (1982).
[5]B. A. Brown *et al.*, Phys. Rev. C **26**, 2247 (1982).
[6]R. J. Seestrom-Morris *et al.*, Phys. Rev. C **31**, 923 (1985).
[7]J. L. Ullmann *et al.*, Phys. Rev. C **31**, 177 (1985).
[8]R. R. Kiziah *et al.*, Phys. Rev. C **30**, 1643 (1984).
[9]C. L. Morris *et al.*, Phys. Rev. C **24**, 231 (1981).
[10]H. A. Thiessen and S. Sobottka, Los Alamos Scientific Laboratory Report No. LA-4534 MS, 1970.
[11]C. L. Morris, computer program FIT (unpublished).
[12]D. E. Alburger, Nucl. Data Sheets **45**, 557 (1985).
[13]D. E. Alburger, Nucl. Data Sheets **42**, 369 (1984).
[14]J. R. Beene, Nucl. Data Sheets **25**, 235 (1978).
[15]H. Verheul and R. L. Auble, Nucl. Data Sheets **23**, 455 (1978).
[16]R. L. Auble, Nucl. Data Sheets **20**, 253 (1977).
[17]G. R. Burleson and J. F. Amann, computer program CROSS (unpublished).
[18]G. Rowe, M. Salomon, and R. H. Landau, Phys. Rev. C **18**, 584 (1978).
[19]R. A. Eisenstein and G. A. Miller, Comput. Phys. Commun. **11**, 95 (1976).
[20]L. S. Kisslinger, Phys. Rev. **98**, 761 (1955).
[21]W. B. Cottingame and D. B. Holtkamp, Phys. Rev. Lett. **45**, 1828 (1980).
[22]C. W. DeJager, H. DeVries, and C. DeVries, At. Data Nucl. Data Tables **14**, 479 (1974).
[23]J. Heisenberg, J. S. McCarthy, and I. Sick, Nucl. Phys. **A164**, 353 (1971).
[24]J. Bellicard, P. Barreau, and D. Blum, Nucl. Phys. **60**, 319 (1964).
[25]G. D. Alkhazov *et al.*, Nucl. Phys. **A274**, 443 (1976).
[26]C. Olmer *et al.*, Phys. Rev. C **21**, 254 (1980).
[27]L. J. Tassie and F. C. Barker, Phys. Rev. **111**, 940 (1958).
[28]A. M. Bernstein, V. R. Brown, and V. A. Madsen, Comments Nucl. Part. Phys. **11**, 203 (1983).
[29]A. M. Bernstein, V. R. Brown, and V. A. Madsen, Phys. Lett. **71B**, 48 (1977).
[30]P. M. Endt, At. Data Nucl. Data Tables **23**, 547 (1979).
[31]J. D. Zumbro, EPICS working group meeting, 1986 (unpublished).
[32]J. W. Lightbody *et al.*, Phys. Rev. C **27**, 113 (1983).
[33]M. J. LeVine, E. K. Warburton, and D. Schwalm, Phys. Rev. C **23**, 244 (1981).